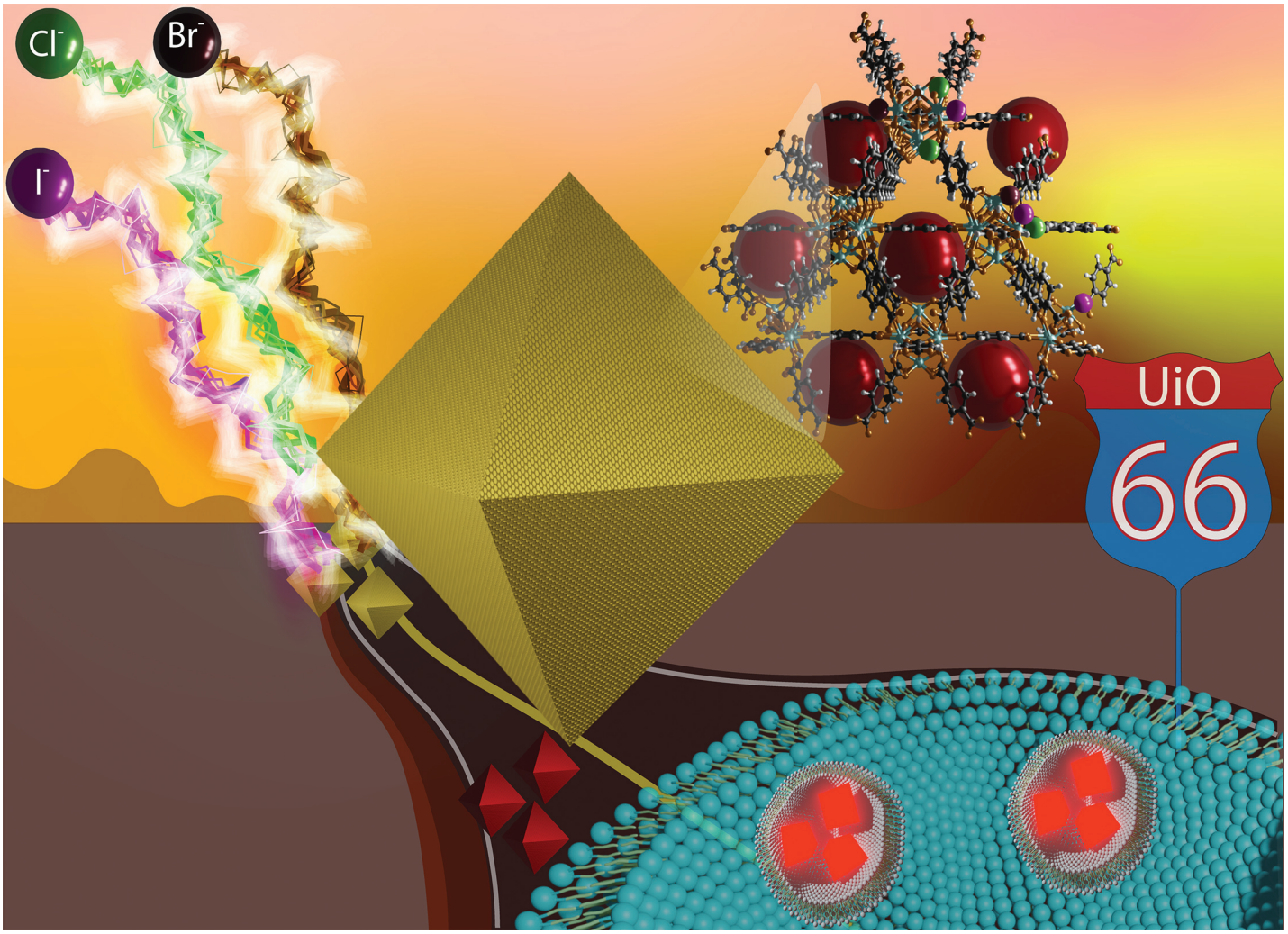

Showcasing research from Dr. Beatriz Pelaz's group at the Center of Chemical Biology and Molecular Materials (CiQUS), University of Santiago de Compostela, Santiago de Compostela, Spain.

High-yield halide-assisted synthesis of metal–organic framework UiO-based nanocarriers

The synthesis of nanosized metal-organic frameworks (NMOFs) is a requisite for their application as injectable drug-delivery systems. The co-modulator role of halide ions has been demonstrated to produce UiO-66-NMOFs (< 100 nm) with precise morphology and good reaction yield. The resulting NMOFs exhibit sustained colloidal stability in biologically relevant media. As a model, they were loaded with Rhodamine-6G (R6G), which remained trapped in biologically milieu. The R6G-loaded-NMOFs were efficiently internalized by cells without impairing cell viability.

As featured in:

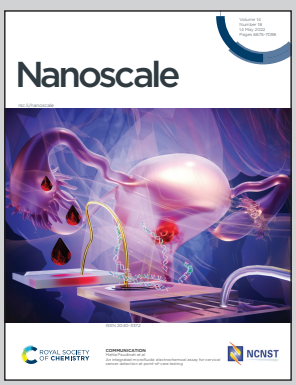

See Pablo del Pino, Beatriz Pelaz *et al.*, *Nanoscale*, 2022, **14**, 6789.

ROYAL SOCIETY OF CHEMISTRY

rsc.li/nanoscale

Registered charity number: 207890

Nanoscale

PAPER

View Article Online
View Journal | View Issue

Cite this: *Nanoscale*, 2022, **14**, 6789

High-yield halide-assisted synthesis of metal–organic framework UiO-based nanocarriers†

Manuel Ceballos, [a] Manuela Cedrún-Morales, [a] Manuel Rodríguez-Pérez, [b] Samuel Funes-Hernando, [b] José Manuel Vila-Fungueiriño, [b] Giulia Zampini, [b] Maria F. Navarro Poupard, [b] Ester Polo, [c] Pablo del Pino *[a] and Beatriz Pelaz *[d]

Received 17th December 2021,
Accepted 15th March 2022

DOI: 10.1039/d1nr08305h

rsc.li/nanoscale

The synthesis of nanosized metal–organic frameworks (NMOFs) is requisite for their application as injectable drug delivery systems (DDSs) and other biorelevant purposes. Herein, we have critically examined the role of different synthetic parameters leading to the production of UiO-66 crystals smaller than 100 nm. Of note, we demonstrate the co-modulator role conferred by halide ions, not only to produce NMOFs with precise morphology and size, but also to significantly improve the reaction yield. The resulting NMOFs are highly crystalline and exhibit sustained colloidal stability in different biologically relevant media. As a proof of concept, these NMOFs were loaded with Rhodamine 6G (R6G), which remained trapped in most common biologically relevant media. When incubated with living mammalian cells, the R6G-loaded NMOFs were efficiently internalized and did not impair cell viability even at relatively high doses.

Introduction

Metal–organic frameworks (MOFs) are a prolific family of porous materials built using 3D extended networks comprising metallic centres coordinated to ligands. These materials have raised considerable interest due to their unique physicochemical properties, particularly motivated by the presence of ordered voids with defined sizes and chemical environments as designed by their constituents.[1,2] These materials have been successfully applied with manifold purposes such as gas storage/separation, drug delivery, catalysis, chemical sensing, and water treatment.[1,3,4]

For the application of MOFs in the life sciences, fine control over size and morphology is desired generally. Producing particles with dimensions below 100 nm is sought to favour the interaction between cells and particles, as well as to avoid vascular blockage when administered intravenously.[5,6] Many studies in the field of nanomedicine have proved that sizes around 50 nm are optimal to favour the internalization of nanoparticles (NPs) by cells.[7] Likewise, producing small, colloidally stable, and homogenous nanoMOFs (NMOFs) is desired for this type of bioapplication.

Reduced size not only has a positive impact on their potential interaction with living entities but also provides interesting properties compared with their bulk counterparts, such as accelerated adsorption/desorption kinetics and higher accessibility to the internal active sites.[1] All in all, during recent years the production of NMOFs has experienced an exponential evolution.[1,2,8]

UiO-66 is among the most studied MOFs due to its high stability, both thermal and hydrolytic. The chemical formula of UiO-66 is $[Zr_6O_4(OH)_4L_6]_n$, which leads to the formation of a porous crystalline extended network.[9] It is noteworthy that UiO-66 is commonly used for engineering defects in its structure as it can bear a high number of defects while keeping its structure.[9–11]

The solvothermal synthesis of the UiO-66 family, assisted by different modulators, has been extensively studied, including carboxylated modulators such as formic acid (FA), acetic acid (AA), trifluoroacetic acid (TFA), and benzoic acid (BA), and non-carboxylated modulators such as water and hydrochloric acid.[12] The growth, kinetics, size and shape of the formed particles are highly influenced by the Zr precursors, *i.e.*, $ZrCl_4$ or

[a]*Centro Singular de Investigación en Química Biolóxica e Materiais Moleculares (CiQUS), Departamento de Física de Partículas, Universidade de Santiago de Compostela, 15782 Santiago de Compostela, Spain. E-mail: pablo.delpino@usc.es*
[b]*Centro Singular de Investigación en Química Biolóxica e Materiais Moleculares (CiQUS), Universidade de Santiago de Compostela, 15782 Santiago de Compostela, Spain*
[c]*Centro Singular de Investigación en Química Biolóxica e Materiais Moleculares (CiQUS), Departamento de Bioquímica, Universidade de Santiago de Compostela, 15782 Santiago de Compostela, Spain*
[d]*Centro Singular de Investigación en Química Biolóxica e Materiais Moleculares (CiQUS), Departamento de Química Inorgánica, Universidade de Santiago de Compostela, 15782 Santiago de Compostela, Spain. E-mail: beatriz.pelaz@usc.es*

†Electronic supplementary information (ESI) available. See DOI: **https://doi.org/10.1039/d1nr08305h**

$ZrOCl_2$, because of the different kinds of Zr-clusters that can be formed. The use of $ZrOCl_2$ leads to faster crystallization as the hydrolysis product is the Zr tetramer $Zr_4(OH)_8(H_2O)_{16}$ instead of the hexanuclear cluster $[Zr_6O_4(OH)_4]^{12+}$.[13,14]

In order to control the MOF size, several relevant chemical equilibria during the crystal growth process have to be taken into account, including the linker deprotonation, the modulator deprotonation, the linker complexation, and the termination.[15] These equilibria are achieved while the crystals grow following the LaMer model.[16] Experimentally several key parameters have been identified, such as the modulator identity and concentration, the equivalents of linker and modulator and the metal–ligand bond interactions.[15,17]

For example, Behrens *et al.*[18] prepared *ca.* 200 nm octahedral UiO-66 particles using a monocarboxylate agent (BA) at high equivalents ratio, as a competitor of the linker. They decreased the equivalents of BA to reduce the size of the MOFs. On the other hand, when the synthesis was performed using a high number of equivalents of BA, the particles presented an irregular shape and size of several microns. Similar observations have found that UiO-66 using lower modulator equivalents in the case of AA, FA, TFA, and dichloroacetic acid (DCA). In these cases, at very low modulator equivalents (<50 eq.), UiO-66 NMOFs under 100 nm have been produced.[15,19]

On another note, it is well known that acidic species, such as hydrochloric acid, inhibit the linker deprotonation, increasing the reaction yield.[20] Yet these species can also hydrolyse *N*,*N*-dimethylformamide (DMF), typically used as a solvent during these synthetic methods,[21] forming FA in the media that can also act as a modulator.

The effect of the precursor and modulator on the crystallinity, structural defects and porosity has been widely investigated. However, their impact on the production of UiO-66 NMOFs, particularly aminated-derivate NMOFs, remains unclear. Several attempts to produce UiO-66-NH_2 NMOFs with reduced size have led to NMOFs around 100 nm by changing the modulator and the reagent ratios.[22] The smallest NMOFs produced following these strategies used a mixture of BA and AA in a ratio of 20 : 3.75 with respect to $ZrCl_4$ and 2-aminoterephthalic acid (NH_2–BDC), in a solvothermal synthesis kept at 120 °C during 24 hours.[23]

In the present work, we report the effect of several synthetic parameters in order to produce UiO-66-NH_2 NMOFs with sizes below 100 nm, aiming for their application as a drug delivery system (DDS). Specifically, we have explored the influence of the Zr precursor and the modulator, and the role of halides as co-modulators (Scheme 1), which was also confirmed. The resulting UiO-66-NH_2 NMOFs (see Table 1) were colloidally stable in biologically relevant media and were efficiently internalized by living cells without impairing cell viability. As a proof of concept, they were loaded with Rhodamine 6G (R6G), a potent mitochondrial probe.[24,25] The loading rate and the

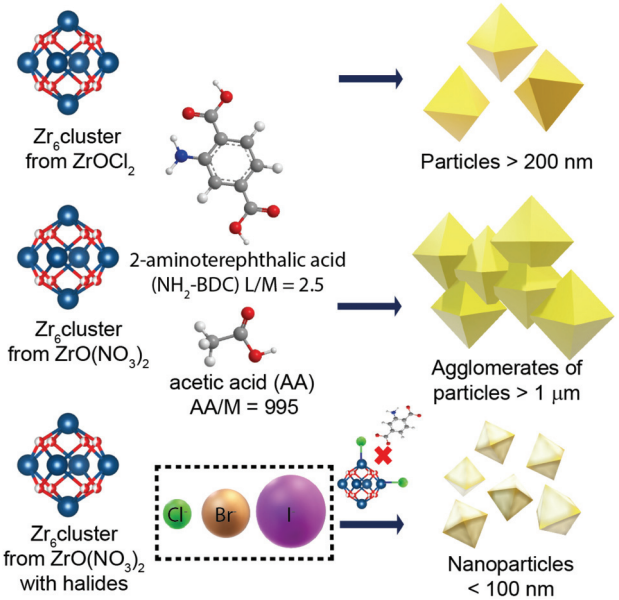

Scheme 1 Summary of the studied parameters and their effect during the synthesis of UiO-66-NH_2.

Table 1 Summary table of samples prepared

Name	Zr precursor	Ligand	Co-modulator	Size (nm)
UiO-66-NH_2($ZrOCl_2$)	$ZrOCl_2$	NH_2–BDC	—	225 ± 37
UiO-66-NH_2	$ZrO(NO_3)_2$	NH_2–BDC	—	>1000
UiO-66-NH_2:Cl^-	$ZrO(NO_3)_2$	NH_2–BDC	Cl^-	94 ± 10
UiO-66-NH_2:Br^-	$ZrO(NO_3)_2$	NH_2–BDC	Br^-	81 ± 9
UiO-66-NH_2:I^-	$ZrO(NO_3)_2$	NH_2–BDC	I^-	109 ± 14
UiO-66($ZrOCl_2$)	$ZrOCl_2$	BDC	—	186 ± 13
UiO-66	$ZrO(NO_3)_2$	BDC	—	>1000
UiO-66:Cl^-	$ZrO(NO_3)_2$	BDC	Cl^-	174 ± 13

Beatriz Pelaz

*Dr Beatriz Pelaz is currently an ERC-StG grantee, Ramón y Cajal researcher and Principal Investigator at the Center of Chemical Biology and Molecular Materials (CiQUS, University of Santiago de Compostela). She received her Ph.D. from the University of Zaragoza (2012). Then she was a postdoctoral fellow at the Philipp-Universität Marburg. Since 2017, she has co-led the BioNanoTools (**https://www.usc.es/ciqus/es/grupos/bionanotools**) group in CiQUS. The research of her group is focused in the development of remotely controlled smart materials, and the study of their interaction with living entities.*

stability of R6G were evaluated before studying the internalization rate of the NMOFs.

Results and discussion

Influence of zirconium precursor

In order to produce UiO-66-NH_2 NMOFs, as a starting point, $ZrOCl_2$, NH_2–BDC and AA were used as the Zr source, ligand and modulator, respectively, using a molar ratio of 1 : 2.5 : 995, herein kept constant unless otherwise specified (see the Experimental section). The first parameter that we varied was the Zr source, *i.e.*, $ZrO(NO_3)_2$ instead of $ZrOCl_2$. While the Zr cluster (*i.e.* tetramer) produced by $ZrOCl_2$ favours the kinetic growth of the MOF, the impact of $ZrO(NO_3)_2$ (which forms as a cluster the extended oligomer $Zr_8O_{28}(NO_3)_8$)[26] has been previously studied in terms of the product crystallinity, regardless of how it influences the size and shape of the MOFs.[27,28] We observed that using $ZrOCl_2$ leads to octahedral crystals with a well-defined shape and facets but a broad size distribution, ranging from 200 to 400 nm (see Fig. 1a and Fig. S1 and S2 of the ESI†). In the case of $ZrO(NO_3)_2$, the formation of twinned particles can be related to the cluster formed, as shown in Fig. 1b (see Fig. S1 and S2†). As the Zr stoichiometry for the cluster formed with oxynitrate precursor is double that in the case of the oxychloride one, we hypothesized that during MOF crystal growth several facets grow simultaneously, leading to the formation of octahedral particles.

Influence of the modulator rate

Aiming to prevent the formation of twinned particles, while using the $ZrO(NO_3)_2$ precursor, the modulator equivalents were varied around our standard conditions (*i.e.*, 995 equivalents of AA, 1.8 mL), using the following volumes (equivalents) of AA: 1.4, 1.6, 1.8, 2.0 and 2.2 mL (775, 885, 995, 1105 and 1215 equivalents of AA, respectively). As shown in Fig. S3,† the variation of modulator equivalents in this range appears uninfluential with respect to the size or morphology of the NMOFs formed. In particular, in all cases we obtained twinned particles.

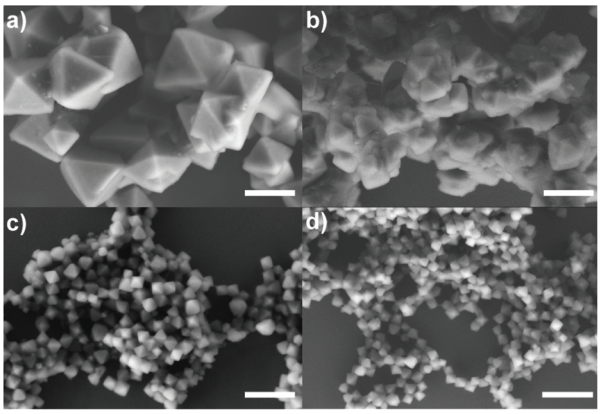

Fig. 1 Representative micrographs of the UiO-66-NH_2 particles obtained using (a) $ZrOCl_2$ or (b) $ZrO(NO_3)_2$ as Zr precursor; or using the combination of (c) $ZrO(NO_3)_2$ and HCl; and (d) $ZrO(NO_3)_2$ and NaCl. Scale bars correspond to 500 nm.

Influence of the chloride as a co-modulator

The results from the influence of the two first parameters led us to conclude that the chlorine ions present in the $ZrOCl_2$ precursor were involved in the crystal growth of the particles. Thus, the effect of chloride as a co-modulator was investigated by adding it externally during the synthesis while using the precursor $ZrO(NO_3)_2$. We expected to produce particles with a defined morphology (*i.e.*, octahedral) as occurred when using $ZrOCl_2$. To confirm this hypothesis, we selected two different chlorine sources, *i.e.*, hydrochloric acid (Fig. 1c) and sodium chloride (Fig. 1d), at a fixed ratio of 1 : 17 $Zr : Cl^-$, leading to discrete nanocrystals with a size less than 100 nm.

HCl has previously been identified as responsible for improving the reaction yield and reducing reaction times for the synthesis of UiO-66 and UiO-67.[13,20] Goesten *et al.*[29] argued that this fact was surprising when $ZrCl_4$ was used as a precursor, considering that upon the precursor hydrolysis more HCl is produced in the media during the MOF growth. One might think that HCl neutralization would have been a parameter to improve the speed and the synthesis yield instead of the opposite.[29] In this direction, Mu *et al.*[30] related the typically small UiO-66 crystal size (around 200 nm) to the partial ligand deprotonation as a result of the increment of protons in the solution during synthesis. They used FA, hypothesizing that it was responsible for the partial protonation of BDC on the MOF surface, leading to the generation of discrete particles. When a deprotonating agent such as triethylamine (TEA) was added, twinned particles were formed instead of octahedral ones.[30] As discussed, in our case, the use of the same amount of Cl^- ions from different sources led us to the same result, which was octahedral NMOFs of less than 100 nm. This result demonstrates that the pH effect is not a critical factor here, confirming that chlorine ions play an active role, preventing the generation of twinned particles, and more importantly, allowing us to get discrete particles with sizes below 100 nm.

Influence of different halides as co-modulators to produce UiO-66-NH_2 NMOFs

Some reports have investigated the role of different dihalides or halides such as iodine and fluoride.[31,32] In the case of iodine, its reaction with thiol ligands to form UiO-66-SH has been studied. Iodine can form an RS–I bond. However, this reaction prevents the MOF oxidation, thereby increasing its stability.[31] For fluoride ions, it has been reported that it is capable of strongly interacting with the metal site,[32] acting as blocking agents for carboxylated ligands and breaking the $Zr_8O_{28}(NO_3)_8$ oligomer formed by the oxynitrate precursor.[26]

The anion effect in Zr–MOF has already been investigated by Reinsch *et al.*[33] They reported that sulphate and dichromate anions coordinate to the metal positions in the Zr cluster, leaving available just eight of the twelve positions for the

linker coordination. This led to the formation of UiO-66 with an incomplete number of ligands, which is very frequent.

Therefore, we decided to systematically study the role of the different halides (X^-) in the synthesis of UiO-66-NH_2 NMOFs. For that, we established a common synthetic condition using $ZrO(NO_3)_2$ as a Zr source and the corresponding sodium halide (NaX) salts, which are, sodium fluoride, sodium chloride, sodium bromide, and sodium iodide, while fixing the ratio $Zr:X^-$. As previously discussed, the Zr oxychloride (Fig. 2a) and the oxynitrate precursors (Fig. 2b) led to octahedra with broad size distribution (200–400 nm) and large twinned microparticles, respectively; these samples will be referred to as UiO-66-NH_2 ($ZrOCl_2$) and UiO-66-NH_2, respectively (see Table 1).

Keeping constant the molar ratio of halide used during the UiO-66-NH_2 NMOF synthesis, the previously observed morphology (octahedral and not-twinned particles) and size range (*i.e.*, 80–90 nm) observed using different chloride sources (Fig. 1c and d) were maintained in the case of chloride, bromide, and iodide ions (Fig. 2c, d and e, respectively; Fig. S4 and S5† for additional SEM and TEM images; Fig. S6† shows the aspect of the solutions in methanol). The halide-assisted NMOFs will be denoted as UiO-66-NH_2:Cl^-; UiO-66-NH_2:Br^- and UiO-66-NH_2:I^- for the samples assisted by chlorine, bromine and iodine, respectively; they showed average sizes of 94 ± 10 nm, 81 ± 9 nm, and 109 ± 14 nm (Table 1 and Fig. S7†), respectively, as measured from SEM micrographs. We ascribe the slightly larger size of UiO-66-NH_2:I^- to the partial oxidation of iodide in the presence of NO_3^- ions ($E^\circ_{Cl_2/Cl^-} = 1.396\,V$, $E^\circ_{Br_2/Br^-} = 1.098\,V$, $E^\circ_{I_2/I^-} = 0.0620\,V$, and $E^\circ_{-NO_3^-/NO_2-} = 0.0940\,V$), decreasing the amount of this co-modulator and increasing the size of the NMOFs.

For completeness, we also tried NaF as a co-modulator, which however prevented the formation of particles. We

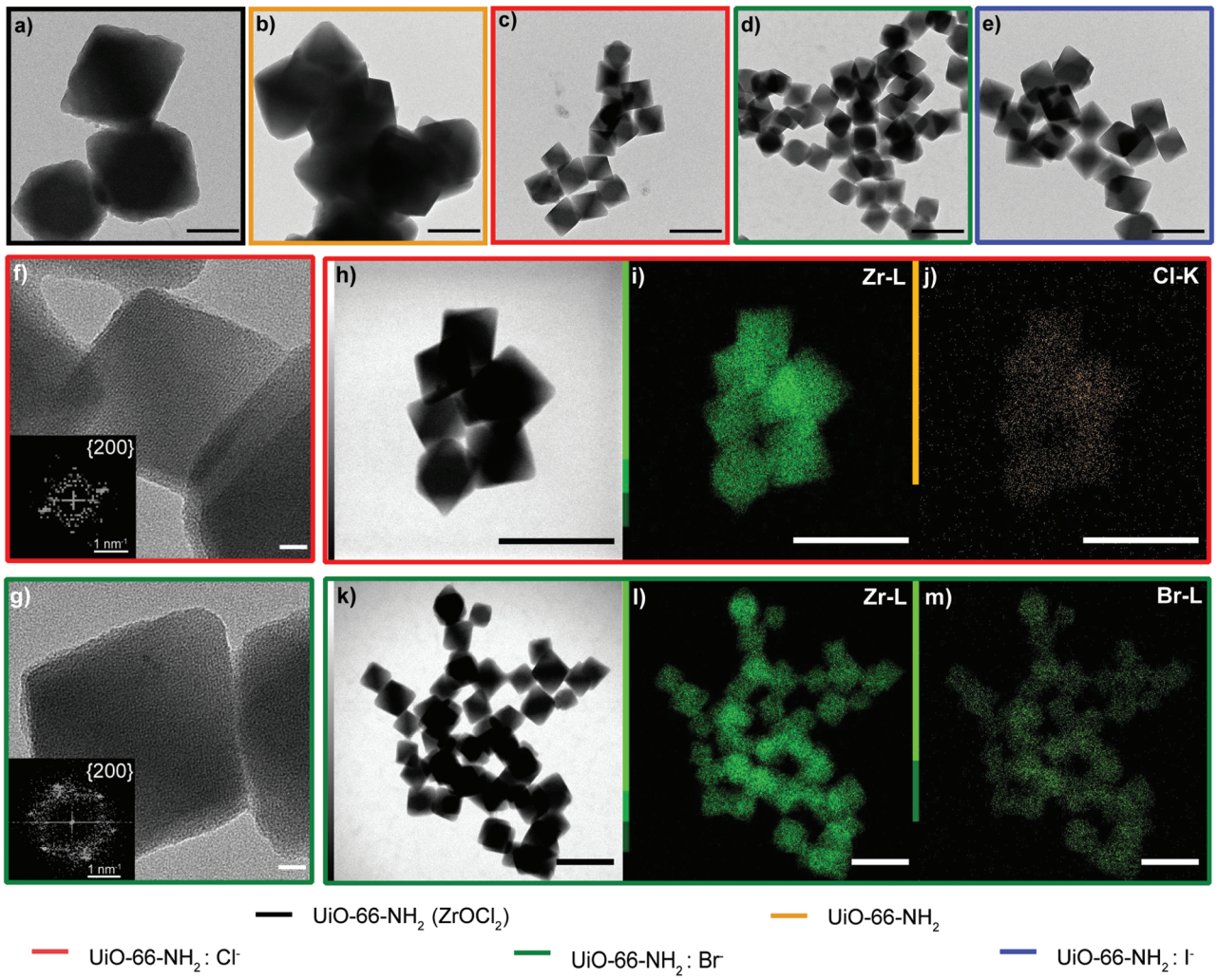

Fig. 2 TEM images of (a) UiO-66-NH_2 ($ZrOCl_2$) (black), (b) UiO-66-NH_2 (orange), (c) UiO-66-NH_2:Cl^- (red), (d) UiO-66-NH_2:Br^- (green), and (e) UiO-66-NH_2:I^- (blue), HRTEM of (f) UiO-66-NH_2:Cl^- and (g) of UiO-66-NH_2:Br^- and (h–j) STEM-EDX images of UiO-66-NH_2:Cl^- (h) with Zr (i) and Cl^- (j) mapping, and (k–m) STEM-EDX images of UiO-66-NH_2:Br^- (k) STEM, Zr (l) and Br^- (m) mapping. Scale bars correspond to 200 nm except for the HRTEM images, in which they correspond to 10 nm.

hypothesize that fluorine ions coordinate to the zirconium cluster, preventing further crystal growth. This hypothesis was confirmed by measuring the UV–vis spectra of the formed clusters using all the halides (Fig. S8†). Moreover, the formation of a precipitate was observed in the case of the fluoride ions, leading to high scattering in a broad spectral range as a result of the poor solubility of ZrF_4 formed in the solution (Fig. S9†). The results obtained with iodide and bromide confirmed our hypothesis about the critical role of halide ions in the growth of the UiO-66-NH_2 NMOFs.

High-resolution transmission electron microscopy (HRTEM) showed highly crystalline NMOFs; in the case of UiO-66-NH_2:Cl^- and UiO-66-NH_2:Br^-, the fast Fourier transform (FFT) analysis of the corresponding TEM images of single NMOFs showed the characteristic {200} index of the a face-centered-cubic structure of the $Fm\bar{3}m$ space group (insets in Fig. 2f and g). The *d*-spacing, in this case, corresponds to *ca.* 10.78 Å and *ca*. 10.000 Å nm, respectively. These *d*-spacings are in good agreement with the theoretical *d*-spacing (200) for UiO-66, 10.373 Å, and as a consequence with one half of the lattice parameter of the UiO-66 unit cell (Fig. S10 and Table S1†). EDX experiments confirmed, in all the NMOFs, a homogeneous Zr and N distribution (data not shown). In the case of the halides, Cl^- and Br^- ions were detected (Fig. 2j and m, respectively) distributed in all the crystals. However, the I^- was not present in a detectable amount. We hypothesized they were washed out during the washing steps of the NMOFs as their coordination ability was reduced compared with that of Cl^- or Br^-.

Wide-angle X-ray scattering (WAXS) measurements were performed in capillary mode, the main reflections of which were in agreement with previously reported powder X-ray diffraction patterns,[34] and which revealed the presence of broad peaks at low 2θ values, in both the samples containing halides and the sample synthesized with $ZrOCl_2$ (Fig. 3a). To corroborate this broad peak around 4° 2θ, small-angle X-ray scattering (SAXS) measurements were performed (Fig. 3b); these broad peaks have been attributed to the presence of ordered missing cluster defects.[27,35] The intensities of diffracted peaks were reduced, performing a unit-cell refinement with Pawley's method on the diffractogram in Fig. 3a (Fig. S11†), comparing each sample with Pawley's model and the residual, which was less than 1% in all the samples. With this method, the intensities and background were corrected and the cell parameters of each NMOF were calculated and compared with those of a UiO-66-NH_2 cubic cell (Table S2†). The refined cell parameters are in agreement with the reference used to fix the peak position.[35,36]

Fourier-transformed infrared spectra (FTIR) of the samples were compared with that of pure NH_2–BDC as a reference (Fig. 4a–c). The C=O vibration at 1671 cm^{-1} was shifted for all the experiments to 1558 cm^{-1} for the samples synthesized with $ZrO(NO_3)_2$, and to 1555 cm^{-1} for UiO-66-NH_2($ZrOCl_2$). It is well known that the vibrations of the bands for UiO-66-NH_2($ZrOCl_2$) are less intense than those for UiO-66-NH_2:X^- (X^-: Cl^-, Br^- and I^-), in particular compared with UiO-66-NH_2:

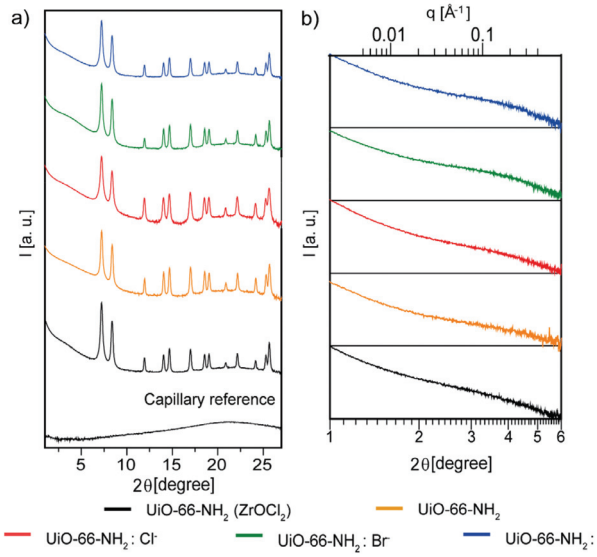

Fig. 3 Crystallographic characterization of UiO-66-NH_2 NMOFs: UiO-66-NH_2 ($ZrOCl_2$) (black), UiO-66-NH_2 (orange), UiO-66-NH_2:Cl^- (red), UiO-66-NH_2:Br^- (green) and UiO-66-NH_2:I^- (blue). (a) WAXS analysis measured at a sample-to-detector distance of 288 mm and (b) SAXS analysis measured at a sample-to-detector distance of 1343 mm in capillary mode.

Cl^-; this evidence corroborates the better complexation of the ligand with the Zr cluster in this sample compared with the others, due to the carboxylate anion having two strongly coupled C–O bonds with a Zr cluster.[37,38] The vibrations at 3505 cm^{-1} and 3390 cm^{-1} corresponding to the asymmetric and symmetric stretching of N–H bond were shifted to 3465 cm^{-1} and 3350 cm^{-1} because the complexation changed the chemical environment in the MOF formation.[39,40]

Raman spectra (see Fig. S12†) of the different UiO-66-NH_2 NMOFs samples showed, in all cases, C=C stretching of aromatic rings centered at 1627 cm^{-1}, O–C–O symmetric stretching in-phase at 1425–1447 cm^{-1} and C–O stretching at 1270 cm^{-1} related to the organic linker;[41] and for the metal–ligand coordination signatures, peaks related to Zr–O were observed at 247, 365 and 620 cm^{-1}.[42]

The UV–vis spectra of UiO-66-NH_2:X^- (X^-: Cl^-, Br^- and I^-) (Fig. 4d) show three sharp bands, one at 240 nm, a transition that can be attributed to an electronic transition between the halide and the Zr–O cluster,[43] and two at 270 and 370 nm corresponding to the n–π^* transition of the amine group and the π–π^* transition of the NH_2–BDC and Zr–O clusters,[44] respectively. For UiO-66-NH_2($ZrOCl_2$) the bands shifted slightly to 246, 281 and 392 nm, respectively, due to the bigger particle size. Interestingly, in the case of UiO-66-NH_2, without halide just two bands appeared at 306 and 415 nm, red shifted due to the size of the particles. In this case, the band attributed to the halide at shorter wavelengths was not present.

Thermal gravimetric analysis (TGA) of the samples (Fig. 5a) shows the thermal stability of the MOFs. All of them were stable up to 350 °C, and only UiO-66-NH_2 started to decom-

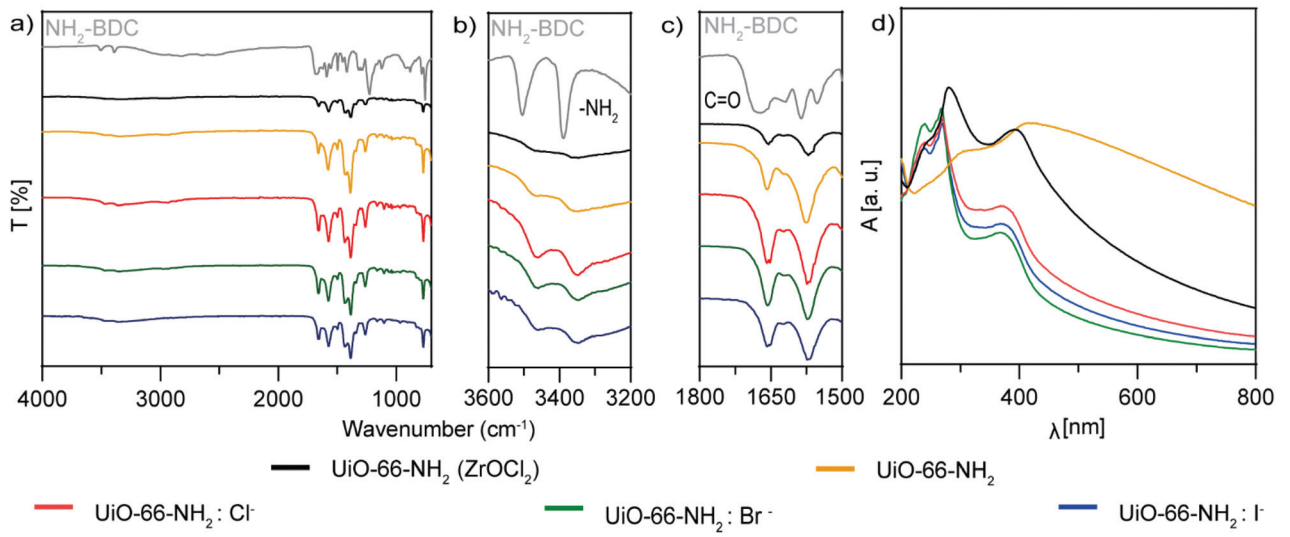

Fig. 4 (a–c) FTIR analysis and (d) UV–vis spectroscopy of UiO-66-NH_2 NMOFs: UiO-66-NH_2 ($ZrOCl_2$) (black), UiO-66-NH_2 (orange), UiO-66-NH_2:Cl^- (red), UiO-66-NH_2:Br^- (green) and UiO-66-NH_2:I^- (blue).

pose before that temperature. Also, it is interesting to observe that the samples that might be ligand defective are UiO-66-NH_2 and UiO-66-NH_2:I^- (see the ESI†), as indicated by their lower rate compared with the Zr cluster.[45] This is sustained by our observations of an active role of chloride and bromide ions as a part of the crystalline structure of the NMOFs, as iodide ions were not observed in our TEM studies.

N_2 sorption measurements at 77 K show type I isotherms (Fig. 5b), characteristic of microporous materials. The Brunauer–Emmett–Teller-specific surface area (S_{BET}) of UiO66-NH_2 ($ZrOCl_2$) is 865.8 $m^2\ g^{-1}$, whereas the areas of UiO66-NH_2:X^- (X^-: Cl^-, Br^-, I^-) are virtually the same, with values of 1017.7, 1027.9 and 1040.0 $m^2\ g^{-1}$, respectively (Table 2). These findings are in good agreement with results reported elsewhere.[13,46,47]

The lower BET surface area of UiO66-NH_2 ($ZrOCl_2$) can be ascribed to the higher dimension of the particles with respect to that of UiO-66-NH_2:X^- (X^-: Cl^-, Br^-, I^-). Furthermore, the halide samples present very similar values of S_{BET}, indicating the high reproducibility of the synthetic strategy in terms of the precise morphology and size, despite the change in the halide ion.

Inductively coupled plasma optical emission spectroscopy (ICP-OES) measurements were performed for all the samples (Table S3†). These measurements allowed us to determine both the molar concentration and the number of NMOF particles per milliliter. This last calculation was done considering their dimensions as obtained by SEM measurements (see section S2 from the ESI, Table S4†),[48] and on the other hand to determine the zirconium concentration (mg mL^{-1}). Additionally, these measurements allow us to evaluate the reaction yields (Table S3†). An increase in the reaction yield was observed for all the syntheses in which a halide was added. In particular, the yield of the reaction increased from 10% and 34% for UiO-66-NH_2 ($ZrOCl_2$) and UiO-66-NH_2, respectively, to *ca.* 77%, 52% and 45% for UiO-66-NH_2:Cl^-, UiO-66-NH_2:Br^- and UiO-66-NH_2:I^-, respectively. The yield increment was especially significant in the case of the chloride ions, leading to more than twice the amount of MOF than in the equivalent synthesis performed without this halide.

Nanoparticle tracking analysis (NTA) and dynamic light scattering (DLS) experiments were carried out to evaluate the effective hydrodynamic diameter of the NMOFs (Fig. 6a and b). NTA showed that UiO-66-NH_2($ZrOCl_2$) has an effective diameter of *ca.* 200 nm, while for UiO-66-NH_2:X^- (X^-: Cl^-, Br^-, I^-) the effective diameters were below 140 nm (Fig. 6a and Table S5†). These data were in good agreement with the DLS measurements carried out where the hydrodynamic diameter was above 200 nm for 66-NH_2($ZrOCl_2$) and around 150 nm for the samples synthesized with halides (see Fig. 6b, Fig. S13, and Table S5†). For UiO-66-NH_2 the NTA measurements could not be carried out due to its poor colloidal stability and DLS showed hydrodynamic diameters above 700 nm.

ζ-Potential measurement showed values above 5 mV for all the NMOFs (see Fig. 6c, and Table S5†). This is explained by the presence of the amine group from NH_2–BDC as a pendant group.

To complete the characterization of the UiO-66-NH_2 NMOFs, the colloidal stability in different media at different times was studied. The selected media were MilliQ water, lysosomal medium (phagolysosomal simulant fluid (PSF), 0.02 M and pH 5), complete cell media (Dulbecco's Modified Eagle Medium (DMEM) supplemented with 10% foetal bovine serum (FBS)) and phosphate-buffered saline (PBS, 0.1 M, pH 7.4) (Fig. 6d, and Table S6†). UiO-66-NH_2($ZrOCl_2$) NMOFs showed good stability in water, PSF and DMEM, while in PBS an increment in the effective diameter was observed after 1 h, indicating that the NMOFs were aggregating. In the case of UiO-66-NH_2:X^- (X^-: Cl^-, Br^-, I^-), in PFS an increment in size

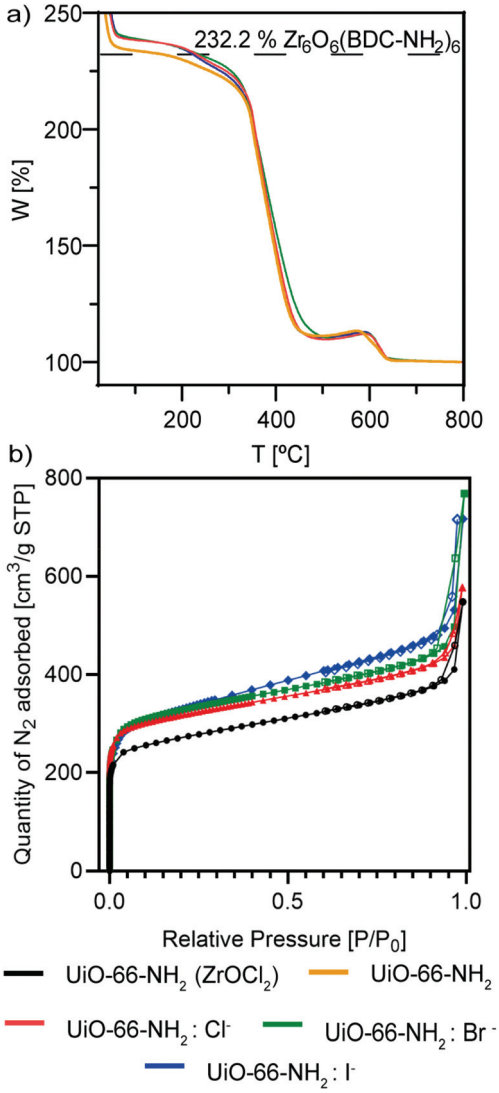

Fig. 5 (a) TGA analysis and (b) BET isotherms of UiO-66-NH_2 NMOFs: UiO-66-NH_2 ($ZrOCl_2$) (black), UiO-66-NH_2 (orange), UiO-66-NH_2:Cl^- (red), UiO-66-NH_2:Br^- (green) and UiO-66-NH_2:I^- (blue).

Table 2 BET specific surface area (S_{BET}) of UiO-66 samples

Sample	S_{BET} ($m^2\ g^{-1}$)
UiO-66-NH_2 ($ZrOCl_2$)	865.8 ± 18.2
UiO-66-NH_2:Cl^-	1017.7 ± 12.0
UiO-66-NH_2:Br^-	1027.9 ± 13.5
UiO-66-NH_2:I^-	1040.0 ± 10.8
UiO-66 ($ZrOCl_2$)	1160.2 ± 13.7
UiO-66:Cl^-	1231.1 ± 13.6

was observed with respect to the samples in water; however, they remained stable along the measured time. For DMEM all samples showed an increment in size consistent with the protein corona formation;[49] finally in PBS the samples showed a similar tendency to UiO-66-NH_2($ZrOCl_2$) but with much lower aggregation rates.

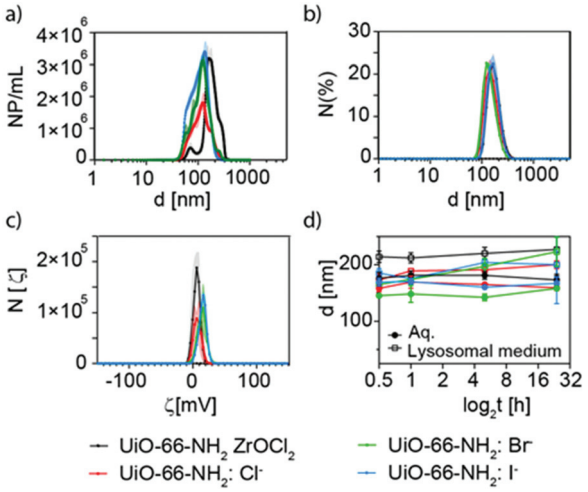

Fig. 6 Effective diameter (hydrodynamic diameter) of UiO-66-NH_2 NMOFs analyzed by (a) NTA and (b) DLS. (c) ζ-Potential measurements. (d) Summary of the stability tests in water and lysosomal medium. Black line corresponds to UiO-66-NH_2 ($ZrOCl_2$), red to UiO-66-NH_2:Cl^-, green to UiO-66-NH_2:Br^- and blue to UiO-66-NH_2:I^-.

These data show that our NMOFs have consistent colloidal stability despite lacking induced defects by the use of a defect-inducer modulator during the synthesis[19,50] or being modified with an additional external surface coating.

Chlorine ions as co-modulators for the UiO-66 NMOF synthesis

For completeness, we studied the synthesis of UiO-66 NMOFs using the same optimized conditions as used for the synthesis of UiO-66-NH_2 NMOF. That is, using both Zr precursors ($ZrOCl_2$ and $Zr(NO_3)_2$) and chlorine ions (NaCl) in the same optimized ratio (see Table 1).

Interestingly, we obtained individual octahedral particles smaller than 200 nm when chloride ions were present on the synthesis, as part of the precursor or added as a salt (UiO-66 $ZrOCl_2$ and UiO-66:Cl^-, Fig. 7a and b). In the absence of chloride ions, the particles obtained were bigger than 800 nm, forming multitwinned particles (Fig. 7c). This result confirms the role of the chloride ions in the generation of small UiO-66 particles. We further performed TEM (Fig. S14 and S15†) and STEM-EDX experiments for UiO-66:Cl^- NMOFs, and chloride ions were detected, showing the same homogeneous distribution in the MOFs (Fig. 7d) as observed for the UiO-66-NH_2:X^- (X^-: Cl^-, Br^-) NMOFs. As previously done with UiO-66-NH_2, we characterized the UiO-66 produced using ICP-OES, UV–vis spectroscopy, DLS, ζ-potential and N_2 sorption (see Fig. S16–S18 and Tables S7 and S8†). UiO-66-NH_2 yielded bigger hydrodynamic diameters and a ζ-potential closer to neutrality. In the case of UiO-66 ($ZrOCl_2$) and UiO-66:Cl^- they showed positive potential values. As expected, the samples presented higher values of S_{BET} with respect to the relative aminated samples, with values of 1160.2 and 1231.1 $m^2\ g^{-1}$ for UiO-66 ($ZrOCl_2$) and UiO-66:Cl^-, respectively (Table 1 and Fig. S19†).

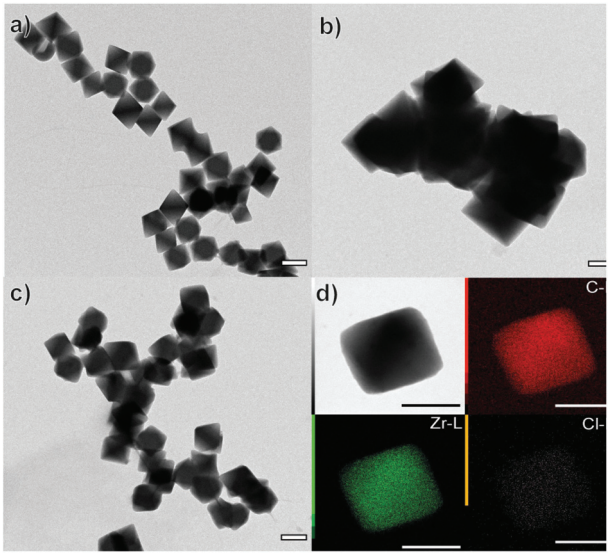

Fig. 7 Representative TEM images of (a) UiO-66 ($ZrOCl_2$) (b) UiO-66 (c) UiO-66:Cl^- and, (d) EDX elemental mapping of carbon, zirconium and chloride from a UiO-66:Cl^- NMOF. Scale bars correspond to 200 nm for TEM and to 100 nm for STEM-EDX.

UiO-66 NMOFs as DDSs

Loading of Rhodamine 6G. The UiO-66 MOF family has been extensively used as DDSs because of their good stability, the low toxicity of their components, and their large porosity. According to its crystal data, UiO-66 has a cage size of 0.75 and 1.2 nm with a pore aperture of 0.6 nm, and different molecules have been encapsulated, such as calcein,[51] dichloroacetate,[52,53] 5-fluorouracil,[52] doxorubicin,[3,54] 5-aminolevulinic acid,[55] *etc*.

As a model molecule, we selected Rhodamine 6G (R6G, Table S9 and Fig. S20†) to evaluate the loading abilities of the synthesized NMOFs. To load the NMOFs, a post-loading strategy was applied by simply mixing the NMOFs with a solution of R6G in a ratio of 1 : 2 Zr : R6G (w : w) (see Table S10†). After thorough washing of the NMOFs, we evaluated the loading rate for UiO-66-NH_2 NMOFs, finding loading rates from 27 to 31%, corresponding to a ratio of *ca.* 0.6 mg R6G per mg Zr and a loading rate of R6G per NMOF on the order of 10^5 per NMOF (see sections S5–S7 of the ESI, Fig. S21 and Table S11†). The loading of R6G increased the hydrodynamic size of the NMOFs while their ζ-potentials were kept positive except for $NH_2(ZrOCl_2)$@R6G, the potential of which was nearly 0 mV (see Fig. S22–S25 and Table S12†). Interestingly, we found similar UiO-loading rates for UiO-66 NMOFs (*ca*. 30% of loading), with a ratio of *ca.* 0.6 mg R6G per mg Zr, corresponding to 6–7 × 10^5 molecules of R6G per NMOF (see Tables S13 and S14, and Fig. S26–S28†). The observed loading ratio corresponds to *ca*. 17–20% w/w for all the synthesized NMOFs, UiO-66-NH_2 and UiO-66.

Despite working with highly crystalline structures, this post-loading efficiency is higher than that previously reported with 5-fluorouracil, in which loadings of about 2%[9] or 5%[52] w/w (in the case of UiO-66-NO_2) were achieved using different synthetic approaches and working with highly defective UiO-66. An extremely high loading of 1 mg doxorubicin per mg MOF was reported by Chen *et al.*[54] and another high loading ratio higher than 25% w/w has been reported, but as a consequence of the incorporation of the drugs as a part of the UiO-66 structure.[9] On the other hand, the number of molecules per NMOF was of the same order of magnitude as the encapsulation of Hoechst or pro-fluorophores in ZIF-8-based nanocomposites previously reported by us.[56,57]

The aim was to use these NMOFs as DDSs to transport the R6G to the intracellular domain of cells. It is well known that most nanomaterials are trapped in lysosomal compartments where they are further degraded.[58,59] NMOFs are not an exception.[56,60,61] We studied the stability of the loading of R6G in different media for different times up to 24 h. We used the same media as previously selected for colloidal stability studies except for PBS, that is, water, complete DMEM, and PSF. The results proved that for UiO-66-NH_2 NMOFs, the R6G encapsulated was stable in MilliQ water with no significant release in any of the samples (see Table S15, and Fig. S29†). However, the time-dependent release of R6G showed a clear increase in the cases of UiO-66-NH_2:Cl^- and UiO-66-NH_2:Br^-, with 1 and 1.8% release at 24 h, respectively, while for the rest the R6G release remained below 0.7%. The same trend was observed in both PSF and DMEM. For PSF, both samples showed a release of *ca.* 3% at 24 h, while for DMEM a higher release was observed close to 4% and 4.5% for UiO-66-NH_2:Cl^- and UiO-66-NH_2:Br^-, respectively.

In the case of UiO-66 the released R6G was higher in all the cases and in all the media, in particular for UiO-66:Cl^- in PSF and DMEM at 24 h releases of *ca*. 14% and 4% were observed (see Table S16†). These results show that the presence of the amine group is uninfluential concerning the loading rate of the NMOFs, yet it stabilizes RG6 within the NMOFs. Additionally, it demonstrates that the encapsulation stability in our NMOFs is very high.

If we compare the cargo release from other UiO-66 nanosystems (please note that we are typically referring to UiO-66 not to UiO-66-NH_2 NMOFs as, for the latter, literature examples are scarce), we find that the release of doxorubicin after 24 h at 37 °C was higher than 20% at pH 5, 6.8 and 7.4, being very close to the 25% at pH 5,[54] while the release of encapsulated calcein from UiO-66 MOFs has been reported to occur at approximately 80% mass release after 5 h in solution.[51]

Cell studies

Next, we evaluated the interaction of UiO-66-NH_2 NMOFs with cells in 2D cell cultures of A549 adenocarcinoma cells. We assessed the biocompatibility using the resazurin test, which confirmed the correct metabolic rate of mitochondria in cell cultures. We used concentrations of up to 100 μg Zr mL^{-1} (which corresponds to *ca.* 320 μg mL^{-1} or 0.82, 2.1, 0.93 and 1.97 nM of UiO-66-NH_2, UiO-66-NH_2:Cl^-, UiO-66-NH_2:Br^-, and UiO-66-NH_2:I^-, respectively), which showed no significant toxicity for any sample after 24 h of incubation (see Fig. S30†). The same result was obtained when testing the UiO-66 NMOFs

(see Fig. S31†) in the same concentration range. These results are in good agreement with previous toxicity tests reported with the UiO-66 family particles.[55] As mentioned above, the biocompatibility of this MOF family is very high, being one of the reasons the reduced toxicity of its components, for example, Zr is one of the rare transition metals that are naturally present in the human body (*ca.* 300 mg of Zr).[51]

After confirming the low toxicity of our NMOFs, we studied the uptake of UiO-66-NH_2 NMOFs using fluorescence microscopy and flow cytometry (Fig. 8, Fig. S32 and Table S17†). To do this, we used the R6G-loaded NMOFs. R6G was selected as cargo for two reasons, (i) to provide the NMOFs with fluorescence to track them intracellularly and (ii) due to its ability to target functional mitochondria.[24,25] Confocal microscopy imaging experiments showed the intracellular location of the NMOF in the perinuclear region, as expected (Fig. 8a).[56,60] This intracellular localization indicates that R6G remains inside the NMOFs, as mitochondria staining is not visible as a result of intracellular R6G leakage. Also, despite presenting a positive ζ-potential, the loaded R6G is not capable of vectorizing the NMOFs to the mitochondria either.

To study the cellular uptake by flow cytometry, 25 pM of UiO-66-NH_2($ZrOCl_2$) and UiO-66-NH_2:X^- (X^-: Cl^-, Br^-, I^-) were incubated for 6 h in complete cell media at 37 °C, 5% CO_2. We found that the cellular uptake was higher for UiO-66-NH_2 ($ZrOCl_2$) compared with UiO-66-NH_2:X^- (X^-: Cl^-, Br^-, I^-), which presented similar internalization rates (see Fig. 8b and c). This difference might be related to the conversion of the concentration of NMOF from mass to molar concentration, as UiO-66-NH_2($ZrOCl_2$) is the sample with a less defined morphology and broader size distribution. However, this difference in the uptake was significantly reduced when the experiment was performed using a constant amount of Zr (2.5 μg mL^{-1}, which corresponds to 8 μg mL^{-1} of NMOF). In this case, the internalization rate was very similar in all cases. We only observed reduced uptake for UiO-66-NH_2:Cl^- NMOFs (see Fig. 8c). These uptake rates are expected based on the physicochemical parameters studied during the characterization of the NMOFs, *i.e.* their hydrodynamic diameters and their ζ-potential values.[62] These results are in good agreement with the results obtained by fluorescence microscopy analysis and evidence the critical impact of per-

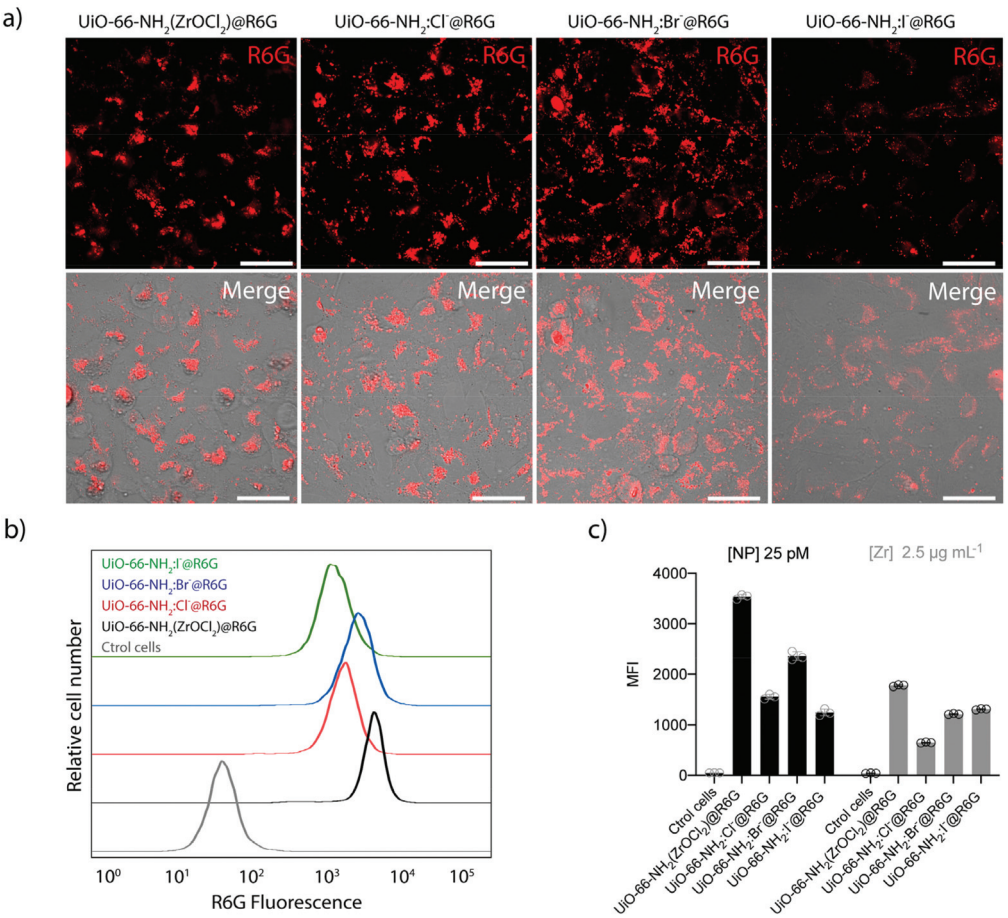

Fig. 8 (a) Representative microscopy confocal images of A549 cells incubated for 6 h with 25 pM of different UiO-66-NH_2@R6G and UiO-66-NH_2:X^-@R6G NMOFs. Scale bars correspond to 25 μm. (b) Flow cytometry analysis of A549 cells exposed to vehicle (PBS) and the different UiO-66-NH_2:X^-@R6G formulations at 25 pM of NMOFs or to 2.5 μg Zr mL^{-1}. Histograms represent experiments done in triplicate. (c) Quantification of R6G fluorescence from flow cytometry analysis in (b). Bars represent means ± SD (n = 3).

forming the experiments using a particular metric or another one.[63]

Conclusions

In this work, we have studied systematically the role of halides as co-modulators to produce UiO-66-NH_2 NMOFs with a size below 100 nm using a new synthetic method. Interestingly, all halides except fluoride ions yielded highly crystalline NMOFs, and their addition improved greatly the reaction yield. In the case of chlorine and bromine, the halide ions were present in the crystalline structure, as confirmed by STEM-EDX experiments. The critical role of halides, in particular of chlorine, in controlling the final particle size was further corroborated by extending our synthetic method to produce UiO-66 NMOFs.

The NMOFs synthesized exhibited great colloidal stability against different pHs, with the presence of proteins or ionic strength maintaining a constant effective diameter. These NMOFs could be post-loaded with *ca*. 17–20% w/w of R6G. The leaking of R6G was negligible up to 24 h in different media with different values of pH (*i.e.* MilliQ water, complete DMEM and PSF).

These NMOFs are highly biocompatible as observed by resazurin assay up to 100 μg mL^{-1} of Zr. The intracellular distribution of the NMOFs was the expected one. The NMOFs were located in the perinuclear region, most likely trapped in lysosomes, as normally happens with nanomaterials having equivalent features. The uptake was evaluated and despite observing a different uptake of UiO-66-NH_2($ZrOCl_2$)@R6G when molar concentrations were considered, when the uptake was compared using the mass of Zr per volume, this difference was minimized, as expected considering their physicochemical features.

Experimental

Materials and reagents

Zirconyl chloride octahydrate ($ZrOCl_2{\cdot}8H_2O$ 98%), zirconyl nitrate trihydrate ($ZrO(NO_3)_2{\cdot}3H_2O$ 99%) and 2-aminoterephthalic ($H_2NC_6H_3$-1,4-$(CO_2H)_2$ 99%, NH_2–BDC) were purchased from Sigma Aldrich. Rhodamine 6G (R6G) was purchased from Alpha Aesar (~95%). All the reagents were used as received.

Synthesis of UiO-66-NH_2 ($ZrOCl_2$), UiO-66-NH_2:X^- (X^-: Cl^-, Br^-, I^-) NMOF and UIO-66 NMOFs. 25 mL of a DMF solution containing 51 mg of $ZrOCl_2{\cdot}8H_2O$ (Sigma Aldrich #224316) or 45 mg of $ZrO(NO_3)_2{\cdot}3H_2O$ (Sigma Aldrich #243493) for UiO-66-NH_2 ($ZrOCl_2$) or UiO-66-NH_2:X^- (X^-: Cl^-, Br^-, I^-), respectively, was taken. Then, 25 mL of DMF containing 72.5 mg of 2-aminoterephthalic acid (NH_2–BDC, Sigma Aldrich #381071) were prepared. Later, a heating plate and the adaptor for the 50 mL vial was prepared at 120 °C. When the temperature had been reached, 5 mL of $ZrOCl_2{\cdot}8H_2O$ (or $ZrO(NO_3)_2{\cdot}3H_2O$) and 5 mL of NH_2–BDC were added to a 50 mL round flask and the mixture was sonicated for 30 seconds. In the case of halide-modulated synthesis, the 50 mL flask contained the corresponding sodium halide salt (32 mg of NaCl (Fisher Scientific #S/3161/60), 56 mg of NaBr (Sigma Aldrich #71329) or 81 mg of NaI (Sigma Aldrich #383112)). Then, 1.8 mL of acetic acid (AA) was added to the solution. After sonication for another 30 seconds, the round flask was placed in the heating plate, and was left at 120 °C overnight.

The sample was collected by centrifugation (10 min, 7100 rcf). Then it is washed 3 times in DMF and 3 times in methanol. Finally, the UiO-66-NH_2 ($ZrOCl_2$) was left in 1 mL of MeOH in an Eppendorf tube.

The same reaction protocol was used but replacing the NH_2–BDC with 66.5 mg (Sigma Aldrich #185361) of BDC to produce UiO-66 and UiO-66:Cl^- NMOFs.

Scanning electron microscopy (SEM). SEM micrographs were obtained using a ZEISS FE-SEM ULTRA Plus after the deposition of a drop of diluted sample onto a piece of clean silicon wafer.

Transmission electron microscopy (TEM). TEM measurements were carried out on a JEOL JEM F200 microscope equipped with a cold-field emission gun operated at 80 kV. TEM images were acquired using a Gatan OneView Camera. EDX analyses were performed with a Centurio Detector. Samples were prepared by adding a drop of diluted samples to a 400 mesh Cu grid and letting them dry.

Wide-angle X-ray scattering (WAXS) and small-angle X-ray scattering (SAXS). WAXS and SAXS measurements were carried out using an Anton Paar SAXSpoint 5.0 equipped with a micro X-ray source of Cu (λ = 0.154 nm) with a 2D Pilatus3 R 1 M detector at 2 different distances – 288 mm for WAXS and 1343 mm for SAXS – in a Hilgenberg brand capillary tube of 1 mm external diameter.

Thermogravimetric analysis (TGA). TGA measurements were carried out using a TA Instruments Inc. SDT Q-600 thermobalance with a general heating profile from 25 to 800 °C and a heating rate of 5 °C min^{-1} under air using a flux of 100 mL min^{-1}. Before the analysis, all the samples were lyophilized and dried at 100 °C.

UV–vis/fluorescence spectroscopy. A Biochrom Libra S60 UV–visible spectrophotometer was used to record the UV–vis absorption spectrum of samples in solution. Fluorescence characterization in solution was performed using an Infinite® 200 PRO Plate reader, Tecan, Switzerland.

Fourier-transformed infrared spectroscopy (FTIR). FTIR measurements were carried out using a PerkinElmer Spectrum Two spectrometer with ATR. The dried powders were placed in the ATR window and analyzed from 700 to 4000 cm^{-1}.

RAMAN spectroscopy. The Raman measurements were performed with a Renishaw inVia Reflex on a glass substrate with a laser beam at 785 nm, with a 50× objective. The samples were irradiated with a power of 10 mW with an acquisition time of 13 s and 4 accumulations. Only the UiO-66-NH_2:Cl^- sample was measured under different conditions – a power of irradiation of 4 mW, an acquisition time of 13 s and 6 accumulations.

ICP-OES. 20 μL of the samples were digested with 480 μL of aqua regia overnight and diluted to 5 mL with HCl 2% v/v. Zirconium quantification was performed on an Agilent 5800 ICP-OES against 1 and 10 ppm standards.

Dynamic light scattering. The hydrodynamic diameter (d_h) and polydispersity index (PDI) of the nanoparticles were determined *via* DLS using a Malvern Zetasizer Nano ZSP equipped with a 10 mW He–Ne laser operating at a wavelength of 633 nm and a fixed scattering angle of 173°.

Nanoparticle tracking analysis (NTA). All the samples were analysed in water using a NanoSight NS300 (Malvern Instrument Ktd) equipped with a 405 nm laser. All measurements were carried out at 24 °C.

N_2 adsorption–desorption analysis. N_2 sorption isotherms at 77 K were measured on a Micromeritics 3Flex Adsorption Analyzer. The samples (about 20–30 mg) were activated overnight under a high vacuum at 90 °C prior to analysis. The specific surface area was extrapolated within the relative pressure (P/P_0, where P_0 is the saturation pressure) interval of 0.05–0.3 by applying the Brunauer, Emmett & Teller (BET) equation.

The data were analyzed using the 3Flex V5.03 software (Micromeritics Instrument Corp., Norcross, GA, United States).

Colloidal stability tests

DLS measurements at different times (up to 24 h) were carried out in different media: MilliQ water, cell culture medium (Dulbecco's Modified Eagle Medium with phenol red, 4.5 g L-1D-glucose, L-glutamine and pyruvate (DMEM Gibco, Thermo Fisher Scientific, Massachusetts, USA) supplemented with 10% fetal bovine serum (Gibco, Thermo Fisher, Massachusetts, USA) and 1% penicillin/streptomycin (P/S, Gibco, Thermo Fisher Scientific, Massachusetts, USA)), phosphate-buffered saline (PBS, 1×, pH = 7.4) and lysosomal medium (phagolysosomal simulant fluid (PSF), pH = 5; PSF (100 mL): 114 mM sodium phosphate dibasic anhydrous, 114 mM sodium chloride, 0.5 mM sodium sulfate anhydrous, 0.2 mM calcium chloride dihydrate, 6 mM glycine and 20 mM potassium hydrogen phthalate).

Encapsulation of Rhodamine 6G. UiO-66-NH_2 was loaded with Rhodamine 6G (R6G, a fluorescent dye widely used to stain cell mitochondria; Rhodamine 6G J62315; Alfa Aesar) just by mixing the UiO-66-NH_2 as dispersed in water (100 μL, 1 mg mL^{-1} Zr) with a solution of R6G in water (100 μL, 2 mg mL^{-1}). The mixture was incubated for 5 days at 80 °C to ensure that the maximum loading was reached regardless of the diffusion kinetics of the dye molecules through the UiO-66-NH_2 pores. Then the excess dye was removed by centrifugation and the UiO-66-NH_2@R6G was washed three times with water in order to remove the R6G that was weakly adsorbed onto the UiO-66-NH_2 surface.

Cargo stability tests. Cargo stability tests were performed at different times (t = 0, 1, 5 and 24 h) in different media: MilliQ water, PSF and DMEM. For the analysis, 100 μL of the samples of UiO-66-NH_2 (1 mg mL^{-1} of Zr) were centrifuged and the pellets was redispersed in 500 μL of the corresponding media for the analysis. At each time point, 100 μL of each sample were centrifuged to remove the supernatant and measure its fluorescence using the same procedure that was used previously to calculate the dye/MOF (see Fig. S21 and S29; Table S16 for UiO-66-NH_2 and Table S17† for the UiO-66).

Cell culture. The A549 (human lung carcinoma) cell line was maintained in culture in Dulbecco's Modified Eagle Medium with phenol red, 4.5 g L-1D-glucose, L-glutamine and pyruvate (DMEM Gibco, Thermo Fisher Scientific, Massachusetts, USA) supplemented with 10% fetal bovine serum (Gibco, Thermo Fisher, Massachusetts, USA) and 1% penicillin/streptomycin (P/S, Gibco, Thermo Fisher Scientific, Massachusetts, USA). Cells were cultured at 37 °C under a 5% CO_2 atmosphere and kept under humid conditions. After reaching 80% confluency, the cells were washed three times with Dulbecco's phosphate buffered saline (PBS, Biowest, France) and passaged after incubation with 0.25% Trypsin–EDTA (Gibco, Thermo Fisher Scientific, Massachusetts, USA).

Resazurin test. A549 cells were seeded (5×10^3 cells per well) in 96-well microplates 24 h prior to their exposure to different NMOFs in a concentration range from 0 to 100 μg mL^{-1} for 24 hours. After that, cells were washed three times with PBS and a freshly prepared solution of 10% v/v resazurin (from a 0.2 mg mL^{-1} stock solution; Sigma Aldrich, USA, #199303-1G) in complete culture medium was added and incubated for 4 h at 37 °C. The fluorescence at 610/20 nm was measured in a microplate reader (Infinite® 200 PRO, Tecan, Switzerland). Viability values represent the mean ± standard deviation of measurements from three wells.

Confocal microscopy imaging. 100 μL containing 5×10^3 A549 cells were seeded in each well of an 18 well-ibiTreat chamber slide (0.34 cm^2 per well, Ibidi, Germany, #81816). Cell were exposed for 6 hours to 50 pM of NMOFs. Cells were washed with PBS and fixed with a 3.7% *p*-formaldehyde solution (Sigma, USA # 47608) for 20 min at RT and imaged in an Andor Dragonfly spinning disk confocal system mounted on a Nikon TiE microscope equipped with a Zyla 4.2 PLUS camera (Andor, Oxford Instruments) and an OKO-lab incubator. The emission filter used for imaging was 561/620 nm under a 561 nm laser excitation. After acquisition, images were analyzed with FIJI software A549.

Flow cytometry experiments. 1×10^4 cells per well were seeded in a 48 well plate (Corning, New York, USA), 24 h prior to their exposure to 25 pM or 2.5 μg mL^{-1} of NMOFs (300 μL) in DMEM for 6 hours. Then, cells were washed three times with PBS and detached by incubating them for 5 minutes with 75 μL of 0.25% trypsin-EDTA which was later neutralized with complete DMEM without phenol red. After that, cell suspensions were transferred to a 96 well plate and analyzed in a Guava easyCyte BG HT flow cytometer (Merck Millipore, Massachusetts, USA) with a forward scatter signal threshold value of 20 000. UiOs-66-NH_2@R6G NMOF uptake was measured *via* fluorescence in the RED-B channel (695/50 nm) and a total of 5000 cells per group (in triplicate) were analyzed (including a control cell group with no NMOF exposure). After acquisition, data were analyzed with Flowjo software.

Author contributions

M. C., M. C.-M., M. F. N. P., S. F.-H. and G. Z. prepared and characterized the materials and peformed data analysis. J. M. V.-F. performed the HRTEM measurements and M. C. the data analysis. M. R.-P. performed the experiments *in vitro*. E. P., P. d. P. and B. P. conceived the idea, designed and supervised the research; and contributed with funding. All authors contributed to results, discussion, and manuscript writing. All authors have given approval to the final version of the manuscript.

Conflicts of interest

There are no conflicts to declare.

Acknowledgements

The authors acknowledge the financial support of the MCIN/AEI (PID2020-119206RB-I00, PID2019-108624RB-I00, RYC-2017-23457, RYC-2019-028238-I), the Xunta de Galicia (ED431F 2017/02, ED431F 2020/11, 2021-CP090, Centro Singular de Investigación de Galicia Accreditation 2019–2022, ED431G 2019/03), the European Union (European Regional Development Fund – ERDF; H2020-MSCA-ITN grant agreement no. 860942; H2020-FET-Open grant agreement no. 899612; H2020-ICT grant agreement no. 10101694 and INTERREG V-A Spain–Portugal, project 0624_2IQBIONEURO_6_E), and the European Research Council (starting grant no. 950421). M.C.-M. thanks the AEI (FPU19/03155). The authors are grateful for the use of RIAIDT-USC analytical facilities.

References

1 X. Cai, Z. Xie, D. Li, M. Kassymova, S.-Q. Zang and H.-L. Jiang, *Coord. Chem. Rev.*, 2020, **417**, 213366.
2 E. A. Flügel, A. Ranft, F. Haase and B. V. Lotsch, *J. Mater. Chem.*, 2012, **22**, 10119–10133.
3 A. Hashemzadeh, G. P. C. Drummen, A. Avan, M. Darroudi, M. Khazaei, R. Khajavian, A. Rangrazi and M. Mirzaei, *J. Mater. Chem. B*, 2021, **9**, 3967–3982.
4 F. Demir Duman and R. S. Forgan, *J. Mater. Chem. B*, 2021, **9**, 3423–3449.
5 E. Blanco, H. Shen and M. Ferrari, *Nat. Biotechnol.*, 2015, **33**, 941–951.
6 W. Poon, B. R. Kingston, B. Ouyang, W. Ngo and W. C. W. Chan, *Nat. Nanotechnol.*, 2020, **15**, 819–829.
7 L. Shang, K. Nienhaus and G. U. Nienhaus, *J. Nanobiotechnol.*, 2014, **12**, 5.
8 M. B. Majewski, H. Noh, T. Islamoglu and O. K. Farha, *J. Mater. Chem. A*, 2018, **6**, 7338–7350.
9 I. Abánades Lázaro, C. J. R. Wells and R. S. Forgan, *Angew. Chem., Int. Ed.*, 2020, **59**, 5211–5217.
10 X. Feng, J. Hajek, H. S. Jena, G. Wang, S. K. P. Veerapandian, R. Morent, N. De Geyter, K. Leyssens, A. E. J. Hoffman, V. Meynen, C. Marquez, D. E. De Vos, V. Van Speybroeck, K. Leus and P. Van Der Voort, *J. Am. Chem. Soc.*, 2020, **142**, 3174–3183.
11 I. A. Lázaro, N. Almora-Barrios, S. Tatay and C. Martí-Gastaldo, *Chem. Sci.*, 2021, **12**, 2586–2593.
12 R. Wei, C. A. Gaggioli, G. Li, T. Islamoglu, Z. Zhang, P. Yu, O. K. Farha, C. J. Cramer, L. Gagliardi, D. Yang and B. C. Gates, *Chem. Mater.*, 2019, **31**, 1655–1663.
13 M. Taddei, J. A. Van Bokhoven and M. Ranocchiari, *Inorg. Chem.*, 2020, **59**, 7860–7868.
14 A. Clearfield and P. A. Vaughan, *Acta Crystallogr.*, 1956, **9**, 555–558.
15 C. R. Marshall, S. A. Staudhammer and C. K. Brozek, *Chem. Sci.*, 2019, **10**, 9396–9408.
16 S. Wang, C. M. McGuirk, A. d'Aquino, J. A. Mason and C. A. Mirkin, *Adv. Mater.*, 2018, **30**, 1800202.
17 X.-G. Wang, Q. Cheng, Y. Yu and X.-Z. Zhang, *Angew. Chem., Int. Ed.*, 2018, **57**, 7836–7840.
18 A. Schaate, P. Roy, A. Godt, J. Lippke, F. Waltz, M. Wiebcke and P. Behrens, *Chem. – Eur. J.*, 2011, **17**, 6643–6651.
19 W. Morris, S. Wang, D. Cho, E. Auyeung, P. Li, O. K. Farha and C. A. Mirkin, *ACS Appl. Mater. Interfaces*, 2017, **9**, 33413–33418.
20 M. J. Katz, Z. J. Brown, Y. J. Colón, P. W. Siu, K. A. Scheidt, R. Q. Snurr, J. T. Hupp and O. K. Farha, *Chem. Commun.*, 2013, **49**, 9449–9451.
21 G. C. Shearer, J. G. Vitillo, S. Bordiga, S. Svelle, U. Olsbye and K. P. Lillerud, *Chem. Mater.*, 2016, **28**, 7190–7193.
22 X. Fang, S. Wu, Y. Wu, W. Yang, Y. Li, J. He, P. Hong, M. Nie, C. Xie, Z. Wu, K. Zhang, L. Kong and J. Liu, *Appl. Surf. Sci.*, 2020, **518**, 146226.
23 J.-D. Xiao, Q. Shang, Y. Xiong, Q. Zhang, Y. Luo, S.-H. Yu and H.-L. Jiang, *Angew. Chem., Int. Ed.*, 2016, **55**, 9389–9393.
24 C. Ma, F. Xia and S. O. Kelley, *Bioconjugate Chem.*, 2020, **31**, 2650–2667.
25 S. Samanta, Y. He, A. Sharma, J. Kim, W. Pan, Z. Yang, J. Li, W. Yan, L. Liu, J. Qu and J. S. Kim, *Chem*, 2019, **5**, 1697–1726.
26 H. Xu, S. Sommer, N. L. N. Broge, J. Gao and B. B. Iversen, *Chem. – Eur. J.*, 2019, **25**, 2051–2058.
27 Z. Chen, X. Wang, H. Noh, G. Ayoub, G. W. Peterson, C. T. Buru, T. Islamoglu and O. K. Farha, *CrystEngComm*, 2019, **21**, 2409–2415.
28 Z. Chen, X. Wang, T. Islamoglu and O. K. Farha, *Inorganics*, 2019, **7**, 56.
29 M. G. Goesten, M. F. De Lange, A. I. Olivos-Suarez, A. V. Bavykina, P. Serra-Crespo, C. Krywka, F. M. Bickelhaupt, F. Kapteijn and J. Gascon, *Nat. Commun.*, 2016, **7**, 1–8.
30 B. Shan, J. B. James, M. R. Armstrong, E. C. Close, P. A. Letham, K. Nikkhah, Y. S. Lin and B. Mu, *J. Phys. Chem. C*, 2018, **122**, 2200–2206.
31 K. K. Yee, Y. L. Wong and Z. Xu, *Dalton Trans.*, 2016, **45**, 5334–5338.

32 K. Y. A. Lin, Y. T. Liu and S. Y. Chen, *J. Colloid Interface Sci.*, 2016, **461**, 79–87.
33 H. Reinsch, I. Stassen, B. Bueken, A. Lieb, R. Ameloot and D. De Vos, *CrystEngComm*, 2015, **17**, 331–337.
34 H. Zeng, Z. Yu, L. Shao, X. Li, M. Zhu, Y. Liu, X. Feng and X. Zhu, *Chem. Eng. J.*, 2021, **403**, 126281.
35 Y. Ma, X. Han, S. Xu, Z. Wang, W. Li, I. da Silva, S. Chansai, D. Lee, Y. Zou, M. Nikiel, P. Manuel, A. M. Sheveleva, F. Tuna, E. J. L. McInnes, Y. Cheng, S. Rudić, A. J. Ramirez-Cuesta, S. J. Haigh, C. Hardacre, M. Schröder and S. Yang, *J. Am. Chem. Soc.*, 2021, **143**, 10977–10985.
36 M. J. Cliffe, W. Wan, X. Zou, P. A. Chater, A. K. Kleppe, M. G. Tucker, H. Wilhelm, N. P. Funnell, F.-X. Coudert and A. L. Goodwin, *Nat. Commun.*, 2014, **5**, 4176.
37 Y. Du, X. Li, X. Lv and Q. Jia, *ACS Appl. Mater. Interfaces*, 2017, **9**, 30925–30932.
38 M. Pintado-Sierra, A. M. Rasero-Almansa, A. Corma, M. Iglesias and F. Sánchez, *J. Catal.*, 2013, **299**, 137–145.
39 J. Hou, Y. Luan, J. Tang, A. M. Wensley, M. Yang and Y. Lu, *J. Mol. Catal. A: Chem.*, 2015, **407**, 53–59.
40 Y. Jiang, C. Liu, J. Caro and A. Huang, *Microporous Mesoporous Mater.*, 2019, **274**, 203–211.
41 D. B. Dwyer, D. T. Lee, S. Boyer, W. E. Bernier, G. N. Parsons and W. E. Jones, *ACS Appl. Mater. Interfaces*, 2018, **10**, 25794–25803.
42 S. Safa, M. Khajeh, A. Reza Oveisi and R. Azimirad, *Chem. Phys. Lett.*, 2021, **762**, 138129.
43 Y. Feng, Q. Chen, M. Cao, N. Ling and J. Yao, *ACS Appl. Nano Mater.*, 2019, **2**, 5973–5980.
44 S. Subudhi, G. Swain, S. P. Tripathy and K. Parida, *Inorg. Chem.*, 2020, **59**, 9824–9837.
45 G. C. Shearer, S. Chavan, S. Bordiga, S. Svelle, U. Olsbye and K. P. Lillerud, *Chem. Mater.*, 2016, **28**, 3749–3761.
46 K. Užarević, T. C. Wang, S.-Y. Moon, A. M. Fidelli, J. T. Hupp, O. K. Farha and T. Friščić, *Chem. Commun.*, 2016, **52**, 2133–2136.
47 H. Molavi, A. Eskandari, A. Shojaei and S. A. Mousavi, *Microporous Mesoporous Mater.*, 2018, **257**, 193–201.
48 J. Hühn, C. Carrillo-Carrion, M. G. Soliman, C. Pfeiffer, D. Valdeperez, A. Masood, I. Chakraborty, L. Zhu, M. Gallego, Y. Zhao, M. Carril, N. Feliu, A. Escudero, A. M. Alkilany, B. Pelaz, P. D. Pino and W. J. Parak, *Chem. Mater.*, 2017, **29**, 399–461.
49 B. Pelaz, P. Del Pino, P. Maffre, R. Hartmann, M. Gallego, S. Rivera-Fernandez, J. M. de la Fuente, G. U. Nienhaus and W. J. Parak, *ACS Nano*, 2015, **9**, 6996–7008.
50 S. Haddad, I. Abánades Lázaro, M. Fantham, A. Mishra, J. Silvestre-Albero, J. W. M. Osterrieth, G. S. Kaminski Schierle, C. F. Kaminski, R. S. Forgan and D. Fairen-Jimenez, *J. Am. Chem. Soc.*, 2020, **142**, 6661–6674.
51 C. Orellana-Tavra, E. F. Baxter, T. Tian, T. D. Bennett, N. K. H. Slater, A. K. Cheetham and D. Fairen-Jimenez, *Chem. Commun.*, 2015, **51**, 13878–13881.
52 I. Abánades Lázaro, S. Abánades Lázaro and R. S. Forgan, *Chem. Commun.*, 2018, **54**, 2792–2795.
53 I. Abánades Lázaro, S. Haddad, J. M. Rodrigo-Muñoz, C. Orellana-Tavra, V. del Pozo, D. Fairen-Jimenez and R. S. Forgan, *ACS Appl. Mater. Interfaces*, 2018, **10**, 5255–5268.
54 D. Chen, D. Yang, C. A. Dougherty, W. Lu, H. Wu, X. He, T. Cai, M. E. Van Dort, B. D. Ross and H. Hong, *ACS Nano*, 2017, **11**, 4315–4327.
55 Y. Pan, Z. Luo, X. Wang, Q. Chen, J. Chen, Y. Guan, D. Liu, H. Xu and J. Liu, *Dalton Trans.*, 2020, **49**, 5291–5301.
56 C. Carrillo-Carrión, R. Martínez, M. F. Navarro Poupard, B. Pelaz, E. Polo, A. Arenas-Vivo, A. Olgiati, P. Taboada, M. G. Soliman, Ú. Catalán, S. Fernández-Castillejo, R. Solà, W. J. Parak, P. Horcajada, R. A. Alvarez-Puebla and P. del Pino, *Angew. Chem., Int. Ed.*, 2019, **58**, 7078–7082.
57 C. Carrillo-Carrión, R. Martínez, E. Polo, M. Tomás-Gamasa, P. Destito, M. Ceballos, B. Pelaz, F. López, J. L. Mascareñas and P. D. Pino, *ACS Nano*, 2021, **15**, 16924–16933.
58 E. Polo, M. Collado, B. Pelaz and P. del Pino, *ACS Nano*, 2017, **11**, 2397–2402.
59 B. Pelaz, C. Alexiou, R. A. A. Puebla, F. Alves, A. M. Andrews, S. Ashraf, L. P. Balogh, L. Ballerini, A. Bestetti, C. Brendel, S. Bosi, M. Carril, W. C. W. Chan, C. Chen, X. Chen, X. Chen, Z. Cheng, D. Cui, J. Du, C. Dullin, A. Escudero, N. Feliu, M. Gao, M. George, Y. Gogotsi, A. Grünweller, Z. Gu, N. Halas, N. Hampp, R. K. Hartmann, M. C. Hersam, P. Hunziker, J. Jian, X. Jiang, P. Jungebluth, P. Kadhiresan, K. Kataoka, A. Khademhosseini, J. Kopecek, N. A. Kotov, H. F. Krug, D. S. Lee, C.-M. Lehr, K. W. Leong, X.-J. Liang, M. L. Lim, L. M. L. Marzán, X. Ma, P. Macchiarini, H. Meng, H. Möhwald, P. Mulvaney, A. E. Nel, S. Nie, P. Nordlander, T. Okano, J. Oliveira, T. H. Park, R. M. Penner, M. Prato, V. Puntes, V. M. Rotello, A. Samarakoon, R. E. Schaak, Y. Shen, S. Sjöqvist, A. G. Skirtach, M. G. Soliman, M. M. Stevens, H.-W. Sung, B. Z. Tang, R. Tietze, B. N. Udugama, J. S. VanEpps, T. Weil, P. S. Weiss, I. Willner, Y. Wu, L. Yang, Z. Yue, Q. Zhang, Q. Zhang, X. E. Zhang, Y. Zhao, X. Zhou and W. J. Parak, *ACS Nano*, 2017, **11**, 2313–2381.
60 R. Martínez, C. Carrillo-Carrión, P. Destito, A. Alvarez, M. Tomás-Gamasa, B. Pelaz, F. Lopez, J. L. Mascareñas and P. del Pino, *Cell Rep. Phys. Sci.*, 2020, **1**, 100076.
61 C. Orellana-Tavra, S. A. Mercado and D. Fairen-Jimenez, *Adv. Healthcare Mater.*, 2016, **5**, 2261–2270.
62 M. Xu, M. G. Soliman, X. Sun, B. Pelaz, N. Feliu, W. J. Parak and S. Liu, *ACS Nano*, 2018, **12**, 10104–10113.
63 N. Feliu, B. Pelaz, Q. Zhang, P. del Pino, A. Nyström and W. J. Parak, *Wiley Interdiscip. Rev.: Nanomed. Nanobiotechnol.*, 2016, **8**, 479–492.